Shear-enhanced compaction band identification at the laboratory scale using acoustic and full-field methods

Elli-Maria Charalampidou [a], Stephen A. Hall [b], Sergei Stanchits [c], Gioacchino Viggiani [d], Helen Lewis [e]

[a] GFZ German Research Centre for Geosciences, Telegrafenberg D423, 14473 Potsdam, Germany
Telephone number: +49 331 288 1384, Fax number: +49 331 288 1328, Email address: elmachar@gfz-potsdam.de.

[b] Division of Solid Mechanics, Lund University, Lund, Sweden and European Spallation Source AB, Lund, Sweden

[c] TerraTek A Schlumberger Company, 1935 Fremont Drive, 84104 Salt Lake City, USA

[d] Grenoble-INP/UJF-Grenoble 1/CNRS UMR 5521, Laboratoire 3SR, Grenoble, France

[e] Institute of Petroleum Engineering, Heriot-Watt University, Edinburgh EH14 4AS, Scotland, United Kingdom

Abstract:

This paper presents results from the analysis of shear-enhanced compaction bands that developed in a porous sandstone during triaxial compression tests at high confining pressures. The analysis uses non-destructive full-field experimental methods: x-ray tomography, 3D-volumetric Digital Image Correlation (DIC) and Acoustic Emission (AE) monitoring including source mechanisms analysis. The 3D-volumetric DIC measurements reveal that these bands are zones with: a small component of band-parallel slip; a larger component of vertical shortening; compactant volumetric strains; and high maximum shear strains. Low x-ray tomography gray-scale standard deviation values within the bands indicate regions of grain size reduction and grain fragmentation. AE hypocenters detected during loading were concentrated inside these narrow bands and showed predominantly pure and hybrid collapse mechanisms; the latter implies some shear strain and is consistent with the oblique geometry of these bands. The experimental results in general support the hypothesis that laboratory developed shear-enhanced compaction bands, at least those studied here, share more characteristics with compaction bands than with compactant shear-bands; these latter deformation features differ from shear-enhanced compaction bands not only in the mechanical behavior, but also in the kinematics and the grain-scale deformation mechanisms.

Keywords: Sandstone, Shear-enhanced compaction bands, Digital Image Correlation, x-ray Tomography, Acoustic Emissions

1. Introduction

Compaction bands, a subset of deformation bands, have only recently been widely recognized in geological outcrops. Published documentation of naturally occurring compaction bands are confined to studies of two Jurassic Aeolian sandstones (see [1] for a

review); the Navajo Sandstone at the East Kaibab Monocline, Utah [2] and the Aztec Sandstone at the Valley of Fire, Nevada [3,4,5]. The deformation features observed by these authors have been identified as either sets of *pure compaction bands* or as *shear-enhanced compaction band sets*. Pure compaction bands are characterized as narrow tabular zones of inelastic deformation, which have accommodated pure compaction (volume loss) with no evidence of shear and according to these authors, have formed normal to the major principal stress direction [2]. Shear-enhanced compaction bands are inferred to form at 38° to 53° relative to the maximum principal stress direction and thus, to accommodate localized compaction oblique to the loading direction [5]. Field observations have demonstrated that shear-enhanced compaction bands are longer than pure compaction bands but their shortening normal to the band width and offset along the band length are similar. Although more intense grain crushing has been documented in shear-enhanced compaction bands, grain fragmentation and grain size reduction exist in both types of compaction bands [6]. Furthermore, both bands are characterized by reduced porosity and permeability [1, 7]. The latter observation strongly suggests that compaction bands could act as baffles to fluid flow and thus have significant implications for hydrocarbon production in subsurface geologic reservoirs and CO_2 disposal into aquifers.

Initial geological outcrop observations of compaction bands have been followed by many experimental investigations at the laboratory scale. Compaction band formation and propagation have been studied experimentally in a variety of porous sandstones, with porosities ranging from 13% [8] to 28% [9], different mineralogical compositions (among others[8, 10, 11, 12]) and a range of grain sizes [12, 13], deformed under triaxial compression at high confining pressures. *Baud et al.* [13] suggested a classification of these laboratory-generated deformation bands based on their width. Discrete compaction bands, with a width equal to three intact grain-sizes, have been described in *Baud et al.* [13], *Fortin et al.* [11], *Louis et al.* [14], *Tembe et al.* [12], *Stanchits et al.* [15], while diffuse compaction bands, with a width of more than three grain-sizes, have been presented in *Baud et al.* [13], *Tembe et al.* [12], *Louis et al.* [14]. All these bands are characterized by porosity reduction, intense grain fragmentation and permeability decrease.

Several theoretical frameworks, based on both field and experimental observations, have been applied to understand the formation and propagation of compaction bands in porous rocks. Compaction bands in rock can be understood as a bifurcation of the inelastic response, and thus their occurrence can be predicted by using the tools of bifurcation analysis

[16, 17, 18, 19, 20]. Although bifurcation analysis appears to be a good theoretical framework for the compaction band study, it is limited in that continuum analysis deals solely with the onset of the constitutive instability in the initially homogeneous material. Therefore, bifurcation theory cannot explain compaction bands or predict their geometrical complexities, including any further micro-scale deformation. Field observations of long linear natural compaction bands suggested the idealized penny shape geometry, which has motivated different micro-mechanical models (anti-crack and inclusion models) analyzed in the framework of linear elastic fracture mechanics [4, 21, 22]. Such models indicate the ways in which the microstructural heterogeneities affect the compaction band initiation and propagation. A combination of processes described both by the bifurcation theory and an anti-crack model has been applied by *Chemenda* [23] to reproduce tabular compaction bands using finite-difference simulations. Micromechanical parameters related to the formation of compaction bands, such as initial porosity, crushing strength and variability of grain size shape and mineralogy, have been taken into account in discrete element approaches to describe their propagation [24, 25, 26].

The goal of this work is to advance our understanding of the micro-processes that may occur during the formation and evolution of compaction bands in porous sandstone subjected to triaxial compression at the laboratory scale, which is a crucial step in expanding knowledge of the larger scale natural systems. We first present the material used and the experimental procedure followed within this study. Results are discussed in terms of a combination of experimental methods, which captured different aspects of the observed deformation features and the deformation mechanisms that occurred.

2. Material and experimental procedure

The experiments presented here were carried out on a sandstone from the Woustviller quarry, in the Vosges Mountains, France, which comprises approximately 93% quartz, 5% microcline, 1% kaolinite, 1% micas, a few oxides, and has an average porosity of 22% [27, 19, 28]. Grains, mean diameter 300 μm, are moderately sorted and have a sub-angular to round shape. The sandstone's pore network tends to be rather heterogeneous, *i.e.*, some of the pores are rather small in certain regions while, less commonly, in other regions the pores have a shape and a size resembling grains. Observations of these grain-shaped pores suggest weathering out of feldspar grains, potentially by chemical alteration to clays and subsequent transported removal. This assumption is supported by observations of chemically altered

feldspars, seen in thin sections [29]. The cement, which binds the grains together, appears mostly as quartz overgrowths.

Five cylindrical specimens with diameters of 40 mm and height of 80 mm were cored normal to the sedimentary bedding plane. Specimens had two opposite flattened surfaces along their height, which facilitated the pre- and post- deformation ultrasonic wave measurements [30]. A Teflon interface was used at the top and bottom of some samples acting as lubricant during the triaxial loading. A circumferential rounded notch (4 mm in depth and 0.8 mm in height) was machined at the mid-height of four out of the five tested specimens. The circumferential notch was filled with a 0.7 mm thickness Teflon O-ring (following [15]), which prevented the Neoprene membrane (that jacketed the specimens during loading) from entering the notch and, thus, reduced the risk of failure of the experiment due to oil leakage through the membrane. In addition, two extra Teflon pieces were used to fill the space around the flattened surfaces of the specimens and so maintain the cylindrical geometry during the triaxial loading.

Triaxial compression experiments under dry conditions were performed on these Vosges sandstone specimens using the triaxial deformation apparatus at GFZ in Potsdam, Germany. This system consists of a servo-hydraulic loading frame from Material Testing Systems (MTS) with a load capacity of 4600 kN and a triaxial cell sustaining a confining pressure up to 200 MPa. An important characteristic of this system is the ability to record acoustic emissions and ultrasonic transmission signals at a number of different positions during the loading of specimens. During the initial phase of isotropic compression, the confining pressure on the specimens was increased from zero to the highest pressure for each given experiment at a constant rate of 1 MPa/min. The subsequent phase of deviatoric loading was performed under constant displacement control at a rate of 20 μm/min (corresponding to a nominal axial strain rate of $2.5\ 10^{-4}\ min^{-1}$). The axial loading during the latter phase was stopped at different axial strain levels for each sample, after which the specimens were fully unloaded. 3D x-ray tomography images were acquired for all the specimens before and after the triaxial compression experiments.

3. Experimental methods

With the occurrence of localized deformation during a loading experiment, such as compaction bands, standard experimental measures during triaxial testing, which obtain a

bulk value for the whole sample, are insufficient to characterize the mechanisms and structural evolution of the material. For this reason there has been an increasing interest in using full-field methods [31, 32, 30, 33, 34, 7] and acoustic methods [35, 11, 15, 36] that permit analysis of the spatio-temporal distribution of mechanical evolution. However, individually such techniques still cannot answer all the questions being posed; therefore in this work a combination of techniques is employed to provide a powerful experimental tool that can capture the onset, evolution and resultant microstructure of localized deformation and to aid in the understanding of the underlying deformation mechanisms. The main advantage of such a combined experimental analysis approach is connected with the different sensitivities and resolutions of each method. In this paper, we show results on Acoustic Emission (AE) monitoring and source mechanisms analysis together with x-ray Tomography and Digital Image Correlation (DIC) from Vosges sandstones specimens.

3.1 Acoustic emission measurements

AEs, produced by the rock specimens as they deformed, were recorded during the triaxial compression experiments (syn-deformation measurements). Fourteen P-wave sensors were glued on the cylindrical surface of each specimen and sealed into the Neoprene jacket using a two-component epoxy. These sensors were composed of PZT disks of 5 mm diameter and 1 mm thickness placed in brass housings; the PZT elements had a thickness-related resonant frequency of 1 MHz. Two P-wave sensors, of the same characteristics, were embedded in the two metallic platens placed at the top and bottom of the specimen during the experiment.

P-wave transmission measurements were made along 50 traces between different transducer pairs and AE signals were monitored throughout each experiment at each transducer. The AE signals were amplified by 40 dB, using Physical Acoustic Corporation (PAC) preamplifiers equipped with 100 kHz high-pass filters (see for details [15]). Eight out of the sixteen P-wave sensors, used for the ultrasonic transmissions, sent a rectangular ultrasonic pulse of 100 V every 30 seconds. During the ultrasonic transmission, these sensors were disconnected from the preamplifiers. Full waveforms of AE data and ultrasonic transmission signals were stored in a 16 channel transient recording system (DaxBox, PRÖKEL, Germany) with an amplitude resolution of 16 bits at 10 MHz sampling rate [37, 15]. All waveforms were recorded in eight internal hard disks of the recording system with no dead time between consecutive signals.

Recorded ultrasonic transmission signals and AE waveforms were separated automatically after each experiment. The P-wave onset-times were picked using an automatic picking algorithm based on the Akaike information criterion [38]. The AE hypocenter locations were calculated by minimizing the travel time residuals using the downhill simplex algorithm [39], considering time-dependent variations in the measured P-wave transmission velocities and applying a 5 layer anisotropic velocity model, which incorporated the P-wave velocities from five pairs of sensors and those from the vertical sensors [37]. The estimated accuracy of the AE hypocenter locations was of 2 mm. Note that in this paper only the AE analysis is shown in detail; the ultrasonic transmission data were just used, in this case, for the velocity model for hypocenter determination.

First motion amplitudes of the located AE events were picked automatically and first motion polarities were used to define the AE source types by estimating the prevailing source movement [40]. The polarity of each individual event was calculated as the mean of all signed first motion amplitudes, recorded by the array of AE sensors (the convention used is that compressional or dilatational first motions are associated with 'movement' towards or away from the sensors, respectively). According to [40], AE events were described as T-type (tensile) for -1≤polarity <-0.25 (compressional first motions, *i.e.*, 'movement' away from the source), as S-type (shear) for -0.25≤polarity ≤+0.25, and as C-type (collapse) for +0.25≤polarity <+1 (dilatational first-motions, *i.e.*, 'movement' towards the source). Here, we further consider pure C-type to have polarity =+1 and hybrid C-type to have +0.25< polarity <+1. Source type events were plotted together with the AE hypocenter locations.

3.2 X-ray Computed Tomography

3D x-ray tomography images of all the specimens were acquired at the x-ray scanning facility of Laboratoire 3SR, in Grenoble, France before (pre-deformation) and after (post-deformation) the triaxial compression experiments. Results from high resolution scans (HR) focused only on the region of the localized deformation with the full width of the samples imaged but not the full height; this permitted the acquisition of images with voxel dimensions of about 30x30x30 μm^3.

3.3 Digital Image Correlation

The acquisition of 3D images of the specimens before and after the loading experiments permitted analysis of the 3D displacement and strain fields by 3D-volumetric

Digital Image Correlation (DIC). The code *TomoWarp*, developed at Laboratoire 3SR, was used; this code is described in *Hall et al.* [41] and is based on an approach designed initially for time-lapse analysis of hydrocarbon reservoirs under production using 3D seismic images [42]. DIC is a mathematical tool based on the comparison of two digital images, the reference image (undeformed) and the deformed one. The key assumption is that if the intensity of some pixels (voxels in 3D) from the reference image correlates with those from a region of the deformed one, it is likely that they both represent the same region (*e.g.*, [43]). By finding the shifts that align different subsets of the two images a field of displacements can be derived to map one image to the other.

The key steps of the code *TomoWarp* are as follows: (i) definition of a regular 3D grid of nodes distributed over the pre-deformation x-ray tomography image; (ii) definition of regions centered on each node (the *correlation window*); (iii) assumption that the gray-scale distribution is preserved after deformation and only rigid body translation (characterized by its three components) occurred between the pre-deformation and homologous post-deformation sub-volume (no rotation or deformation of the correlation window is considered); (iv) calculation of a *correlation coefficient* (in this case "semblance", see [44]) for each displacement of the correlation window within an area (the *search window*) around the target node in the post-deformation x-ray image; (v) definition of the discrete displacements, as integer number of voxels, given by the displacement with the maximum correlation; (vi) application of sub-voxel refinement involving finding the maximum of an interpolation function that describes the local 3D variation in the correlation (over a 3x3x3 set of displacements about the best discrete shift). The sub-voxel refinement is necessary as the displacements are rarely integer numbers of voxels and it avoids the resolution of an artificially 'stepped' displacement field that would provide erroneous strain fields (with very high values corresponding to each voxel step and no strains between them). After derivation of the 3D vector-displacement field (with sub-voxel accuracy), the strain field can be derived to provide the Cauchy strain tensor components (ε_{ij}); this calculation is made over 8-point cubic elements of neighboring nodes from the DIC analysis grid. Whilst full tensor strain fields are calculated, these are difficult to show and so the first two invariants of the strain tensor are calculated, *i.e.*, the volumetric strain ($\varepsilon_v = \varepsilon_1 + \varepsilon_2 + \varepsilon_3$) and the maximum value of shear strain on any plane ($\varepsilon_s = \frac{2}{3}[(\varepsilon_1 - \varepsilon_2)^2 + (\varepsilon_2 - \varepsilon_3)^2 + (\varepsilon_3 - \varepsilon_1)^2]^{1/2}$, which is the octahedral shear strain), where ε_1, ε_2 and ε_3 are the major, intermediate and minor

imposed principal strains, respectively. The convention of compactant volumetric strains being positive and dilatant volumetric strains being negative is adopted herein.

4. Results

4.1 Summary of Mechanical Data

The mechanical behavior and failure modes of this Vosges sandstone, under triaxial compression up to 60 MPa confining pressure has been previously well-characterized using standard experimental methods [27, 19, 28]. *Charalampidou* [29] further investigated the characteristics and the involved micro-mechanisms of shear band occurrence in the same sandstone being subjected to triaxial compression from 20 to 50 MPa, using full-field and acoustic measurements. In the following, results from triaxial experiments at relatively higher confining pressures are presented. Five specimens were tested from 130 to 190 MPa. Figure 1 shows the loading curves from all the triaxial compression tests with the stress deviator (q) shown as a function of the axial strain ($q = (\sigma_a - \sigma_r)$, where σ_a and σ_r are the axial stress and the confining pressure, respectively; the latter being constant during the deviatoric loading stage). Note that these stress-strain responses are elemental (*i.e.*, they represent material behaviour) only prior to strain localization. In the presence of localized strain, both stress deviator and axial strain as derived from boundary measurements are only nominal, since they are not homogeneous within the specimen.

Specimens Ve4 and Ve6 were loaded under 130 MPa confining pressure. The loading of the latter specimen was stopped temporarily (0.95% of axial deformation) and continued shortly after. Although the stiffness of both specimens is similar at the beginning of the loading stage, the latter specimen is less resistant after 0.6% of axial deformation. Specimens Ve1 and Ve5 were loaded under 160 MPa confining pressure. The former was the only specimen tested without a circumferential notch, while the latter had such a notch at its mid-height and failed at a lower axial stress level. Specimen Ve7 was loaded under 190 MPa confining pressure.

Strain hardening behavior is observed in all specimens. The maximum stress deviator values decrease with increasing confining pressure, which suggests a cap in the yield surface at this stress level. Note that in these experiments the determination of the critical stress conditions corresponding to compactional deformation was not trivial due to the absence of a clear peak in the stress-strain responses obtained. Additionally, the readings of the axial

gages, attached to the specimen mid-height, were not always reliable during the deviatoric compression part (*i.e.*, one of the strain gages might have failed during the experiment). So it was not easy to get a representative local volumetric strain measurement. Furthermore, the onset of localized deformation could not be obtained following the methodology suggested by *Wong et al.* [45], due to lack of volumetric strain data from the isotropic compression part of the experiments. Reasons for this lack included specimens being tested dry, no strain gauges were used and axial gages were not sufficiently sensitive during that part of the loading. An alternative methodology for the identification of the onset of inelastic deformation of these particular experiments was used [29]. This method combines the mechanical results at the meso-scale (*i.e.*, global displacement recorded at the edges of the specimen and reliable local displacements recorded at the mid-height of the specimen) with the hypocenter locations of the AE analysis (transitional measurements from meso- to micro-scale, *i.e.*, specimen- and grain-scale, respectively). The following sections focus on the acoustic and full-field experimental results from specimen Ve7.

4.2 Acoustic Emissions and Source Mechanisms

Figure 2 shows the spatial distribution of the located AE events during the triaxial loading of specimen Ve7. The stress deviator time history (in seconds) and the cumulative AE number, separated into increasing time intervals moving from left to right, are shown in Figures 2a. Colors change to highlight most recent events. Only AE events with amplitudes larger than 2 V were used for the calculation of the cumulative number of AE events. The number of AE events can be seen to have increased with time, which indicates a cumulative damage process. Additionally, an increase in AE events is also seen during unloading, albeit at a lower rate, which suggests a continued locally heterogeneous stress field promoting AE nucleation in places of local stress concentration. Three 2D projections of the 3D AE hypocenter distributions (one perpendicular and two parallel to the specimen axis) are shown in Figures 2b-2d; only AE events with amplitudes larger than 1 V are plotted. The x-y perpendicular projection of the 3D distributions indicates that AE events were concentrated at the middle height of the specimen (*i.e.*, from 25 mm to 55 mm from the bottom edge). The z-x perpendicular projection shows AE events located at the central section of the specimen (*i.e.*, +/- 2 mm), while the z-y perpendicular projection presents AE events located within a wider section of the specimen (*i.e.*, +/- 10 mm). Damage initially occurred in places close to the notches and propagated inwards and the AE locations suggest deformation band

development in the middle-top section of the specimen. AE activity was also recorded near the top edge boundary.

To investigate the micro-processes that took place during the deformation of specimen Ve7, the located AE events were distinguished between pure C-, hybrid C-, S- and T-type events. Figure 3 depicts the spatial distribution of AE hypocenter locations from specimen Ve7 in terms of global axial strain intervals (0.2% steps up to the maximum axial strain and then up to the end of the deviatoric unloading). The stress deviator history between each step is shown in Figure 3a. Figures 3b show the distribution of AE polarities (mean of first motions) from events with amplitudes larger than 1 V. Background colors represent the polarity limits of each event type (black for pure C-type, red for hybrid C-type, blue for S-type and green for T-type events). Figures 3c-3e show the spatial evolution of these AE events types (with amplitudes larger than 1 V) in one horizontal and two vertical 2D projections (colors coincide with those in Fig. 3b, while the spatial limits of these projections are similar to those shown in Fig. 2b-2d). The number of pure C-type events, which are dominant compared to other event types throughout the test, decreases with increasing axial strain. A considerable number of hybrid C-type events is also observed, which increases with increasing stress deviator. Only few S-type events have been identified during the loading and unloading stage, while T-type events are absent within these amplitude ranges.

A complex network of deformation bands have been developed in specimen Ve7 (Fig. 2c-2d, Fig. 3c-3e). During the initial loading stage (from 0 to 0.2% of axial strain, Fig. 3) AE events were located close to the notches, which acting as stress concentrators (see also [46, 12]) facilitated the early onset of inelastic deformation. Damage in this stage was mainly in the form of C-type events and was concentrated in relatively small bands. With increasing axial strain, new deformation bands nucleated from the notches and propagated towards the top section of the specimen, accompanying the further propagation of the former bands. Pore collapse was still the dominant mechanism (almost 65% of pure C-type events and about 35% of hybrid C-type events in Fig. 3b). Just before the end of the loading stage (from 0.8 to 0.865% of axial strain) the propagation of the initial bands halted and only bands at the top part of the specimen continued to evolve. During the unloading stage, a rather diffuse AE activity can be observed, indicating mainly C-type events nucleated in places of the formerly created bands (however, the number of pure C-type events drops to almost 50%). Although only a few S-type events have been located throughout the whole experiment, the resolved deformation bands are not oriented normal to the maximum shortening direction. Because a

range of different orientations can be observed, these bands cannot be strictly characterized as '*pure compaction bands'* [2, 4, 5]. Furthermore, a hidden shear component is also present in the hybrid C-type events, which show much more compaction than S-type events, but still less than pure C-type events. Therefore, we call the observed deformation bands '*shear-enhanced compaction*' bands; this term will be further explained in the following sections.

4.3 X-ray images

X-ray tomography provides a 3D full-field measurement for mapping the x-ray attenuation throughout the samples and is sensitive primarily to density variations when the photon energy (acquisition parameter) and material atomic number (deformation process) are kept constant [47]. Local decrease or increase in densities, in Vosges sandstone specimens deformed under lower confining pressures (*e.g.*, 20 to 50 MPa), has been associated with compactant or dilatant shear bands (*e.g.*, [28, 19, 30]). However, under higher confining pressures (*e.g.*, 130 to 190 MPa) shear-enhanced compaction bands could not be resolved in the gray-scale images [29]. *Otani et al.* [48] and *Louis et al.* [14] demonstrated that different local statistical measurements of gray-scale values can be used to highlight compaction bands. Here, the calculation of the local standard deviation of gray-scale values over 3D grids of small sub-volumes permitted visualization of the compaction bands in the 3D images.

Figure 4 shows different 2D orthogonal projections of the calculated standard deviation values from specimen Ve7 focusing on a region above and below the notches. Calculations were made throughout the image volume over sub-volumes of 600x600x600 μm^3 at a spacing of 150 µm in every direction. A network of closely spaced deformation bands can be resolved by setting a standard deviation threshold level (in red) from 0.022 to 0.027 (32-bit gray-scale). Standard deviation values higher than 0.027 are displayed in black. Lower standard deviation values inside the bands (as compared to values outside the bands) probably indicate a reduction in grain size via grain fragmentation and crushing to below the voxel size, and thus, a homogenization of the image (as different grains and porosity attenuations are averaged over a voxel to give an average gray-scale, which might be similar over a region). The resolved deformation bands are mostly wavy and have different lengths. These bands are inclined 58° to 88° (mean 70°), to the major imposed principal stress direction. Band width varies from 300 to 1200 µm.

4.4 Digital Image Correlation

Displacement and strain fields have been calculated using DIC analysis of the pre- and post-deformation x-ray tomography images of 30 μm voxel size. To facilitate the DIC analysis, the sandstone specimens were placed at approximately the same position for each x-ray tomography scan (*i.e.*, before and after the triaxial compression experiments). Calculations were made over sub-volumes of 600x600x600 μm^3 at a spacing of 600 μm in every direction (*i.e.*, 2 grain sizes). Figures 5a-5b show cumulative volumetric and maximum shear strain fields at the mid-height of the specimen for four different vertical sections, extracted from the 3D strain images, across specimen Ve7. Figure 5c shows the equivalent cumulative axial displacement fields. The term cumulative is used because the displacement and strain maps were calculated after both the loading and unloading of the specimen and, therefore, refer to the displacement and strain fields measured after the whole experiment. Displacement values correspond to vertical translation of each voxel (30 μm /voxel) after the sub-voxel refinement. Figure 5d shows, in gray, the cumulative hypocenter locations of AE events. The largest amplitude pure C-, hybrid C- and S-type events of the loading stage are highlighted in black, red and blue colors, respectively.

The complex geometry of the developed network of shear-enhanced compaction bands contains both compactant volumetric strains (Fig. 5a, 5e, 5i, 5m) and high values of maximum shear strains (Fig. 5b, 5f, 5j, 5n). In general, the top part of the section (above the notches) shows larger vertical displacements, which gradually change to smaller values above and below the resolved deformation bands. Pure C- and hybrid C-type events are where high compactant and maximum shear strain values are measured.

The inclination angles of shear-enhanced compaction to the major imposed principal stress direction as measured from the strain field maps range from 62° to 82°, with a mean of 68°. Recall that the inclination angle measured from the standard deviation analysis of x-ray images was 70°. Note also that angles of around 45°- 53° to the major imposed principal stress direction are measured in some regions close to the notches. Figures 6a and 6b show the z- and y- components of the displacement fields (vertical and horizontal, respectively) close to the central section of specimen Ve7 (y-z plane, x=28.2 mm), together with the equivalent cumulative spatial distribution of AE hypocenter locations, including both loading and unloading stages. AE events with amplitudes larger than 1 V and 3.16 V are shown as small and large spheres, respectively. Black rectangles refer to regions shown in Fig. 6e-6j. Vertical displacement values gradually decrease in places of AE hypocenter concentrations, which coincide with shear-enhanced compaction bands (Fig. 6a). Horizontal displacement

values are higher close to the surface of the specimen and gradually decrease towards the center of the sample (Fig. 6b). In this case, it is rather difficult to correlate the calculated displacement values with the AE hypocenter locations.

Equivalent cumulative maximum shear and volumetric strain fields are shown in Figures 6c and 6d. Shear-enhanced compaction bands have developed above and below the level of the notch. These bands are characterized by positive volumetric strains (compaction) and relatively high maximum shear strains, and are oriented within the range measured from the equivalent standard deviation maps (Fig.4). Figures 6e-6g and 6h-6j show details of the vertical and horizontal displacement fields of the three regions highlighted in Figures 6a-6b. Small black rectangles correspond to the measured values shown in Figure 6k. The transition of the displacement component values is relatively smooth and is without any strong displacements discontinuities. Figure 6k shows the measured vertical and horizontal displacement values from the regions illustrated in Figures 6e-6g and 6h-6j: note that vertical displacements are usually slightly larger than horizontal. Figures 6l-6n depict the combined vertical and horizontal displacement vectors and show that these vectors can change direction locally.

In order to assess whether the resolved deformation features have a shear component, as was suggested by *Bésuelle* [19], the local normal and tangential displacement components and the displacement gradients at the deformation bands are required. Here, such an analysis would be laborious because the orientations of the resolved bands vary. So to simplify, we assume 2D deformation band geometry (similar to Figure 6). A parametric vectorial analysis of the normal and tangential (to the deformation band) displacement components can then be made based on the principal displacements (along z and y direction and measured by the DIC) and the different orientation angles (a) towards the principal stress direction (see Fig. 7). Such analysis suggests that the tangential displacement (*i.e.*, slip) along bands of any orientation is non-zero when the absolute ratio between the vertical and horizontal principal displacements differs from the tangent of this angle. Figure 7 shows the conditions of shear displacement along 2D deformation bands as a function of the orientation angle a. Red lines indicate the limiting values (conditions for zero slip) of vertical to horizontal principal displacement ratios for the measured orientation angles in specimen Ve7 (from 58° to 88°). Any other displacement ratio always resolves a tangential displacement component inside the resolved deformation band.

Displacement values shown in Figure 6k (corresponding to the small rectangles in Figs. 6g and 6j) have been used to evaluate the above model. The resolved deformation band here (Fig. 6k) is inclined at 71.6°. Using the displacements shown in Figure 6k, the calculated displacement ratio is not equal to the tangent of the angle, implying that tangential displacement is non-zero. In such cases, the accommodated slip (tangential displacement) is always much smaller than the band- normal shortening. Such analysis suggests that the resolved deformation bands share similar characteristics with shear-enhanced compaction bands, since they have accommodated tangential displacement. It should be underlined, though, that the parametric 2D analysis presented here should be expanded to a 3D vectorial analysis, which accounts for all principal displacement vectors.

5. Discussion

Experimental results are summarized and discussed below in the context of whether, and to what extent, the resolved shear-enhanced compaction bands share common characteristics with pure compaction bands, observed in both the laboratory and the field, and what similarities exist between the resolved shear-enhanced compaction bands and compactant shear bands formed in the laboratory (see for more details [30]) or observed in the field.

5.1 Characteristics of the resolved shear-enhanced compaction bands using the combination of acoustic and full-field methods

A network of differently orientated shear-enhanced compaction bands has been resolved in specimen Ve7. AE data indicate that these bands initiated at the notches and propagated towards the center of the specimen. *Stanchits et al.* [15] have shown that similar notch geometry resulted in a single compaction band in Bentheim sandstone. The occurrence of a single compaction band in Benthiem sandstone and multiple bands in this Vosges sandstone, for the same sample geometry, could be attributed to local mineralogical, pore network or grain framework characteristics, or to slight geometric variations in the notch [46]. According to *Lin et al.* [49], notch size and position can determine the positioning of the prevailing damage zone and thus, the position of failure, but the final band deformation characteristics are not greatly influenced, so the change in band number is not regarded as significant.

In this study, the width of resolved shear-enhanced compaction bands varied along their lengths, from 300 to 1200 μm (1-4 grain sizes). Similar widths have been documented in other porous sandstones that developed what have until now been termed compaction bands in the laboratory [46, 11, 14, 12] and in the field [2]. Shear-enhanced compaction bands measured in the Vosges sandstone herein show variable inclination angles towards the major principal stress direction. Based on their orientation, these deformation bands more closely resemble naturally developed shear-enhanced compaction bands, observed in Aztec Sandstone outcrops in the Valley of Fire, Nevada [5] than they do naturally developed pure compaction bands, observed in East Kaibab Monocline [2], which these authors inferred to have formed normal to the maximum principal stress direction. Note that naturally developed wavy compaction bands observed in the field [2] and oblique deformation bands that developed under high confining pressures in porous sandstones at the laboratory scale [11], have been previously referred to as compaction bands. However, they share the salient characteristics of shear-enhanced compaction bands as described here.

Vertical displacement field values measured in this study gradually decrease when passing through places of AE event concentration, which contradicts the assumption that displacements are equally distributed among deformation bands [14]. 2D vectorial analysis along the deformation bands' length indicated non-zero tangential displacements, which is not consistent with pure compaction bands, *i.e.*, bands that lack of any shear displacement [2]. Furthermore, measured band-parallel slip was much smaller than the vertical shortening of these oblique bands. This relationship differs from the naturally generated shear-enhanced compaction bands observed by [5], which are described as bands with equal compaction and shear. However, *Eichhubl et al.* [5] do not claim that equal compaction and shear are a requirement of all shear-enhanced compaction bands.

In this study, higher values of compactant volumetric strains, together with higher maximum shear strains have been measured inside shear-enhanced compaction bands compared to strain values measured outside the bands. Furthermore, low standard deviation values were measured inside the resolved bands, which - in terms of image analysis- indicates homogeneous regions, probably caused by grain fracturing and crushing producing a "grain" size locally smaller than the voxel size of the tomography image.

The micro-mechanisms involved in the onset and evolution of shear-enhanced compaction bands were characterized in this study as dominantly collapse events. Pure C- and hybrid C-type events were linked to local compaction and so porosity reduction. S-type

events were fewer. Similar bands that have been documented in wet triaxially deformed Bleurswiller sandstone specimens [11, 50] were characterized by a bigger number of S-type events. This discrepancy in the shear-type mechanisms might be explained by the different mineralogical composition of the two sandstones and/or the existence of water, which acting as a lubricant could have promoted local slip along the resolved bands. However it is not yet clear if these factors provide an adequate explanation.

5.2 Comparison of the resolved shear-enhanced compaction bands with compactant shear bands

The Vosges sandstone shear-enhanced compaction bands are inclined at a higher angle towards the major imposed principal stress than are compactant shear bands formed in the same sandstone under lower confining pressures [28, 30]. However, it is probable that the two modes of localized deformation are related, being the shear- and compaction-dominated end members of a spectrum. To investigate this and the similarities or differences, acoustic and full-field results from specimens loaded under low and high confining pressures are compared below.

Figure 8a-8d summarizes different AE event types as a function of time for four different specimens, together with the equivalent stress deviator curves. Compactant shear bands developed in specimen Ve2 at 50 MPa confining pressure (Fig. 8d, [30]), while shear-enhanced compaction bands developed in specimens Ve4 and Ve6 subjected to 130 MPa confining pressure (Fig. 8a, 8c [30]), and in specimen Ve7 subjected to 190 MPa (Fig. 8b). Strain softening behavior is observed only in Ve2, while strain hardening took place in Ve4, Ve6 and Ve7.

Pure C- and hybrid C-type events were the dominant mechanisms in shear-enhanced compaction bands. In both Ve6 and Ve7, the number of pure C-type events decreases with time (and deformation), which can be related to the formation of a network of oblique shear-enhanced compaction bands (Fig. 3 and [29, 30]); this is not the case for Ve4 in which shear-enhanced compaction bands were not fully developed [30]. The number of S- and T-type events is relatively low in all specimens. For the compactant shear band case (Ve2 as reported by [29]) the portion and evolution of event types is different. Hybrid C-type events dominate, while the number of S-, pure C- and T- type events is smaller (with S-type being much higher than the C- and T-type events). Subsequently pure-C and hybrid C-type events increase, while S- and T-type events decrease up to the peak stress. A local increase in S- and T-type

events and a local decrease in C-type events are observed during the stress drop, while the post-peak stage is mainly characterized by collapse events. Figures 8e-8h show the histograms of AE polarities from all specimens [29]. A reduced number of pure C-type events and a relatively increased number of S- and T-type events is observed for the compactant shear band (Ve2) compared to shear-enhanced compaction bands (Ve4, Ve6, Ve7). These observations lead to the conclusion that pure C- and hybrid C-type events (with hidden component of shear) are the main mechanisms in shear-enhanced compaction bands, retaining a relatively constant ratio in time. Compactant shear bands, however, are characterized by hybrid C-type events with the number of S- and pure C-type events being bigger and smaller, respectively, than in shear-enhanced compaction bands. S- and hybrid C-type events decrease with increasing number of pure C-type events at the post-peak stage.

Eichhubl et al. [5] compared shear-enhanced compaction bands to compactant shear bands at the field-scale, showing that the latter have a much larger shear offset. Figures 9a-9b show the z- and y- components of the displacement fields from a single section of specimen Ve2 (y-z plane, x=11.4 mm). Black rectangles refer to regions shown in Figures 9e-9g. Figures 9c-9d show the equivalent cumulative maximum shear and volumetric strains for the same projection. In these images, compactant shear bands are characterized by high shear strain values as well as high volumetric strains (compactant or dilatant, for more details, see [29, 30]). Note that the cumulative shear and compactant volumetric strains of the compactant shear bands have higher and lower values, respectively, compared to those calculated inside the shear-enhanced compaction bands. Cumulative vertical displacements of this particular Ve2 section show larger values above and smaller values below the band (Fig. 9a), while cumulative horizontal displacements values are higher close to the surface of the specimen and gradually decrease towards the center of the sample (Fig. 9b), but in an opposite direction to that in shear-enhanced compaction bands (Fig. 6b). The local kinematic conditions more closely resemble those of a normal fault, though the term normal fault applies to a much larger structure in which discrete fault plane parallel slip dominates the kinematics.

Figure 9k summarizes the values of vertical and horizontal displacements measured in sections shown as small black rectangles in Fig. (9e-9j). Figures 9l-9n depict the combined vertical and horizontal displacement vectors shown in Figures 9e-9j. The resolved compactant shear band is oriented 47.6° to the major imposed principal stress direction. Calculations of the accommodated slip (tangential displacement) and the band-oblique

shortening (normal displacement), based on displacement values shown in Figure 9k (Fig. 9e, 9h, and 9g, 9j), indicate that the slip along the band equivalent increases (from top to bottom) reaching locally values up to 127 μm at the top and 475 μm at the bottom band, while the band -oblique shortening decreases in a similar way, having values of about 322 μm at the top and 110 μm at the bottom of the band. The band-parallel slip values in compactant shear bands are always (within this study) much larger than those in shear-enhanced compaction bands (few μm).

From the discussion above it seems that the mechanical behavior, the operative mechanisms and the kinematics differ considerably between shear-enhanced compaction bands and compactant shear bands that developed in Vosges sandstone specimens subjected to triaxial compression under different confining pressures. It appears that shear-enhanced compaction bands, at least those studied here, share more common characteristics with pure compaction bands than they do with compactant shear bands and do not develop such high values of maximum shear strains and of band-parallel slip and such larger number of S-type events as those observed in compactant shear bands.

6. Conclusions

A combination of acoustic and full-field methods (pre-, syn-, and post-deformation) has been applied to better characterize shear-enhanced compaction band evolution in porous sandstone specimens that were deformed under triaxial compression at high confining pressures in the laboratory. Analysis of full-tensor strain fields, derived from the 3D-volumetric DIC displacement fields, has revealed localized zones of compactant volumetric strains and high maximum shear strain, which coincide with narrow zones of AE hypocenter concentrations. These zones map out the locations of the deformation bands. The AE analysis has revealed that pure C-type and hybrid C-type events are the dominant mechanism in the evolution of these features. The latter AE event type also implies a portion of shear, which is consistent with the oblique geometry of the bands. The number of S-type events was relatively low. Small band-parallel slip values have been measured along the bands using 3D-volumtric DIC, although vertical shortening of these oblique bands was more pronounced. Furthermore, low x-ray tomography gray-scale standard deviation values inside these zones suggest grain size reduction and grain fragmentation. Shear-enhanced compaction bands, at least those studied here, have more characteristics in common with pure compaction bands

than with compactant shear bands. The latter differ from the former not only in the mechanical behavior, but also in the kinematics and the grain-scale deformation mechanisms.

The combined use of non-conventional experimental techniques used in this work has provided more insight than is possible from the use of the individual techniques alone, and much more than would be possible from standard experimental analyses. It is worth noting that both the AE and full-field methods used herein are non-destructive, which implies that multiple measurements could be made on the same specimen. Furthermore, they could be applied at any time of the experimental procedure, *e.g.*, before, during and after deformation. This provides the potential of capturing both total and in-situ deformation processes at different scales, linked to the resolution and sensitivity of each method. Furthermore, both methods could resolve the complex compaction band geometry in 3D, which is not possible with 2D thin section analysis. However, microstructural observations from thin sections should provide further, complementary insights into the grain-scale deformation.

Acknowledgements

This work follows on from the experimental work that was carried out in the doctoral work of the first author [29]. The authors would like to thank Teng Fong Wong for his helpful comments. The authors would also like to thank Stefan Gehrmann for the preparation of the Vosges sandstone specimens, and Grzegorz Kwiatek and Fatih Bulut for the fruitful discussions on acoustic methods. Georg Dresen is gratefully acknowledged for the financial support of the experiments carried out in GFZ.

References

[1] Holcomb D, Rudnicki JW, Issen K, Sternolf K. Compaction localisation in the Earth and the laboratory: state of research and research directions. Acta Geotechnica 2007; 2: 1-15.

[2] Mollema PN and Antonellini MA. Compaction bands: a structural analog for anti-mode I cracks in Aeolian sandstone. Tectonophysics 1996; 267:209-228.

[3] Sternlof K, Chapin J, Pollard DD, Durlofsky LJ. Effective permeability in sandstone containing deformation band arrays. AAPG Bull. 2004; 88: 1315–1329.

[4] Sternlof K, Rudnicki JW, Pollard DD. Anticrack-inclusions model for compaction bands in sandstone. J. Geophys. Res. 2005; 110: 1-16, B11403.

[5] Eichhubl P, Hooker JN, Laubach SE. Pure and shear-enhanced compaction bands in Aztec Sandstone. Journal of Structural Geology 2010; 32: 12: 1873-1886.

[6] Fossen H, Schultz R & Torabi A. Conditions and implications for compaction band formation in the Navajo Sandstone, Utah. Journal of Structural Geology 2011; 33: 1477-1490.

[7] Sun WC, Andrade JE, Rudnicki JW, Eichhubl P. Connecting microstructural attributes and permeability from 3D tomographic images of in situ shear-enhanced compaction bands using multiscale computations. Geophys. Res. Lett. 2011; 38, doi:, 10.1029/2011GL047683, 201.

[8] Wu XY, Baud P, Wong TF. Micromechanics of compressive failure and spatial evolution of anisotropic damage in Darley Dale sandstone. Int. J. Rock Mech. Min. Sci. 2000; 37:143-160.

[9] Olsson WA, Holcomb DJ, Rudnicki JW. Compaction Localisation in Porous Sandstones: Implications for Reservoir Mechanics. Oil Gas Sci. Technol.- Rev. IFP 2002; 57: 5: 591-599.

[10] Menéndez B, Zhu W, Wong TF. Micromechanics of brittle faulting and cataclastic flow in Berea sandstone. Journal of Structural Geology 1996; 18: 1:1-16.

[11] Fortin J, Stanchits S, Dresen G, Guéguen Y. Acoustic emission and velocities associated with the formation of compaction bands in sandstones. J. Geophys. Res. 2006; 111: B10203, doi:10.1029/2005JB003854.

[12] Tembe S, Vajdova V, Wong TF, Zhu W. Initiation and propagation of strain localisation in circumferentially notched samples of two porous rocks. J. Geophys. Res. 2006; 111: B02409, doi: 10.1029/2005JB003611.

[13] Baud P, Klein E, Wong TF. Compaction localisation in porous sandstones: spatial evolution of damage and acoustic emission activity. Journal of Structural Geology 2004; 26: 603-624.

[14] Louis L, Wong TF, Baud P, Tembe S. Imaging strain localisation by X-ray computed tomography: discrete compaction bands in Diemelstadt sandstone. Journal of Structural Geology 2006; 28: 762-775.

[15] Stanchits S, Fortin J, Guéguen Y, Dresen G. Initiation and Propagation of Compaction Bands in Dry and Wet Bentheim Sandstone. Pure Appl. Geophys. 2009; 166:843-868.

[16] Olsson WA. Theoretical and experimental investigation of compaction bands in porous rocks. J. Geophys. Res. 1999; 104: B4:7219-7228.

[17] Issen KA & Rudnicki JW. Conditions of compaction bands in porous rocks. J. Geophys. Res. 2000; 105 (B9): 21529-21536.

[18] Issen KA & Rudnicki JW. Theory of compaction Bands in Porous Rocks. Phys. Chem. Earth (A) 2001; 26: 1-2: 95-100.

[19] Bésuelle P. Evolution of strain localisation with stress in a sandstone: brittle to semi-brittle regimes. Phys.Chem. Earth (A) 2001; 26: 1-2:101-106.

[20] Bésuelle P. and Rudnicki JW. Localization: Shear Bands and Compaction bands. In: Mechanics of Fluid-Saturated Rocks, Y Guéguen, M Boutéca, editors. Academic Press ; 2004. pp. 219-321.

[21] Rudnicki JW. Models for compaction band propagation. Geoplogical Society, London, Special Publications 2007; 284: 107-125.

[22] Tembe S, Baud P, Wong TF. Stress conditions for the propagation of discrete compaction bands in porous sandstone. Journal of Geophysical Research 2008; 113: BO9409, doi: 10.1029/2007JB005439.

[23] Chemenda AI. Origin of compaction bands: Anti-crack or constitutive instability? Tectonophysics 2011; 499: 156-164.

[24] Wang B, Chen Y, Wong TF. A discrete element model for the development of compaction localization in granular rock. J. Geophys. Res. 2008; 113: BO3202, doi:10.1029/2006JB004501.

[25] Marketos G, Bolton MD. Compaction bands as observed in DEM simulations. In: Powders and Grains, Herrmann and McNamara, editors. London: Garcia-Rojo, Taylor and Francis Group; 2005. pp. 1405-1408.

[26] Marketos G, Bolton MD. Compaction bands simulated in Discrete Elements Models. Journal of Structural Geology 2009; 31: 479-790.

[27] Bésuelle P. Déformation et Rupture dans les roches tenders et les sols indures: comportement homogène et localisation. PhD Thesis. Université Joseph Fourier, Grenoble; 1999.

[28] Bésuelle P, Desrues J, Raynaud S. Experimental characterisation of the localisation phenomenon inside a Vosges sandstone in a triaxial cell. Int. J. Rock Mech. Min. Sci. 2000; 37: 1223-1237.

[29] Charalampidou EM. Experimental Study of Localised Deformation in Porous Sandstones. PhD Thesis. Heriot Watt University and Université de Grenoble, Edinburgh-Grenoble ; 2011.

[30] Charalampidou EM, Hall SA, Stanchits S, Lewis H, Viggiani G. Characterization of shear and compaction bands in a porous sandstone deformed under triaxial compression. Tectonophysics 2011; 503: 1-2: 8-17.

[31] Viggiani G. & Hall SA. Full-field measurements, a new tool for laboratory experimental geomechanics. In: Fourth Symposium on Deformation Characteristics of Geomaterials, SE Burns, PW Mayne & JC Santamarina, editors. Amsterdam: IOS Press; 2008. pp. 3-26.

[32] Charalampidou EM, Hall SA, Stanchits S, Lewis H, Viggiani G. Characterization of shear and compaction bands in sandstone using X-ray tomography and digital image analysis. In: Advances in Computed Tomography for Geomaterials: GeoX2010, KA Alshibli, AH Reed, editors. ISTE Pub; 2010. pp. 59–66.

[33] Dautriat J, Bornert M, Gland N, Dimanov A, Raphanel J. Localized deformation induced by heterogeneities in porous carbonate analyzed by multi-scale digital image correlation. Tectonophysics 2011; 503: 1-2: 100-116.

[34] Nguyen TL, Hall SA, Vacher P, Viggiani G. Fracture mechanisms in soft rock: identification and quantification of evolving displacement discontinuities by digital image correlation. Tectonophysics 2011; 503: 1-2: 117-128.

[35] Olsson WA and Holcomb DJ. Compaction localization in porous rocks. Geophys. Res. Lett. 2000; 27: 21: 3537-3540.

[36] Graham CC, Stanchits S, Main IG, Dresen G. Comparison of polarity and moment tensor inversion methods for source analysis of acoustic emission data. Int. J. Rock Mech. Min. Sci. 2010; 47: 161-169.

[37] Stanchits S, Dresen G and Vinciguerra S. Ultrasonic velocities, acoustic emission characteristics and crack damage of basalt and granite. Pure Applied Geophys. 2006; 163: 5–6: 975–994.

[38] Leonard M and Kennett BLN. Multi-component autoregressive techniques for the analysis of seismograms. Phys. Earth Planet. Int. 1999; 113:1-4: 247.

[39] Nelder J and Mead R. A simplex method for function minimization. Computer J. 1965; 7: 308-312.

[40] Zang A, Wagner FC, Stanchits S, Dresen G, Andresen R, Haidekker MA. Source analysis of acoustic emissions in Aue granite cores under symmetric and asymmetric compressive loads. Goephys. J., Int. 1998; 135: 1113-1130.

[41] Hall SA, Lenoir N, Viggiani G, Desrues J and Bésuelle P. Strain localization in sand under triaxial loading: characterization by x-ray micro tomography and 3D digital image correlation. In: Proceedings of the 1st International Symposium on Computational Geomechanics (ComGeo I). Juan-les-Pins, Cote d'Azur, France; April 29 – May 1st 2009. p. 239-247

[42] Hall SA. A methodology for 7D warping and deformation monitoring using Time-lapse seismic data. Geophysics 2006; 71: O21–O31.

[43] Quinta Da Fonseca J, Mummery PM, Withers PJ. Full-field strain mapping by optical correlation of micrographs acquired during deformation. Journal of Microscopy 2005; 218: 9-21.

[44] Marfurt KJ, Kirlin RL, Farmer SL, Bahorich MS. 3-D seismic attributes using a semblance-based coherency algorithm. Geophysics 1998; 63: 1150-1165.

[45] Wong TF, David C, Zhu W. The transition from brittle faulting to cataclastic flow in porous sandstones: Mechanical deformation. J. Geophys. Res. 1997; 102: B2: 3009-3025.

[46] Vajdova V and Wong TF. Incremental propagation of discrete compaction bands: Acoustic emission and microstructural observations on circumferentially notched samples of Bentheim. Geophys. Res. Lett. 2003; 30: 14: 1775, doi: 10.1029/2003GL017750.

[47] Baruchel J, Buffiere JY, Maire E, Merle P, Peix G. X-ray tomography in material science. Paris: Hermes Science Publications; 2000.

[48] Otani J, Mukunoki T, Sugawara K. Evaluation of particle crushing in soils using X-ray CT data. Soils and Foundations 2005 ; 45: 99–108.

[49] Lin Q, Fakhimi A, Haggarty M, Labuz JF. Initiation of tensile and mixed-mode fractures in sandstone. Int. J. Rock Mech. Min. Sci. 2009; 46: 489-497.

[50] Fortin J, Stanchits S, Dresen G, Gueguen Y. Acoustic Emissions monitoring during inelastic deformation of porous sandstones: Comparison of three modes of deformation. Pure Appl. Geophys. 2009; 166: 823-841.

Figure captions

Figure 1. Stress deviator plotted versus axial strain (global) from specimens loaded under 130, 160 and 190 MPa.

Figure 2. AE results from specimen Ve7: (a) Stress deviator as a function of the number of AE events in different time intervals; (b) - (d) Maps of AE event locations for the same time intervals viewed perpendicular and parallel to the specimen axis.

Figure 3. AE results from specimen Ve7: (a) Stress deviator as a function of time history for different global axial strain intervals; (b) Histograms of AE polarities; (c) – (e) Maps of AE event locations for the same strain intervals viewed perpendicular and parallel to the specimen axis.

Figure 4. Gray-scale standard deviation values (32-bit gray-scale) from HR x-ray tomography images shown in several vertical slices through specimen Ve7.

Figure 5. Specimen Ve7: (a, e, i, m) Volumetric strain field derived from HR x-ray pre- and post-deformation images; (b, f, j, n) Maximum shear strain field derived from HR x-ray pre- and post-deformation HR x-ray images; (c, g, k, o) Vertical displacement field (principal displacement) calculated from pre- and post-deformation HR x-ray images; (d, h, i, p) AE hypocenter locations during loading and unloading.

Figure 6. (a-b)Vertical and horizontal displacement fields from a 2D section from Ve7; AE hypocenter locations are superimposed on the displacement fields; (c-d) Maximum shear and volumetric strain fields for the same projection; (e-g) Expanded view of the vertical displacement field (see a-d); (h-j) Expanded view of the horizontal displacement field (see a-d); (k) Vertical and horizontal displacement values, in small black rectangles shown in (e-g and h-j); (l-n) Displacement vectors for areas shown in (e-g) and (h-j).

Figure 7. Parametric analysis for the conditions of existence of tangential displacement along different orientation angle (a) principal horizontal and vertical displacement values inside the resolved bands. Red lines indicate the conditions of zero slip based on vertical to horizontal principal displacement ratios for the measured orientation angles in Ve7 (from 58° to 88°).

Figure 8. (a-d) Stress deviator and AE event types versus time for four different specimens. Pure C-, hybrid C-, S- and T-type events are shown in black, red, blue and green colors, respectively. Orange rectangles in (b) represent periods of no recordings. No amplitude grouping has been made. The temporal evolution of different crack types is plotted in moving windows of 400 samples at a step of 100 samples; (e-h) Histograms of AE polarities.

Figure 9. Vertical and horizontal displacement fields from a 2D section from Ve2 (a-b); AE hypocenter locations superimposed on the displacement fields. Maximum shear and volumetric strain fields for the same projection (c-d); (e-g) Detail of the vertical displacement field (see a-d); (h-j) Detail of the horizontal displacement field (see a-d); (k) Vertical and horizontal displacement from the small black rectangles shown in (e-g and h-j); (l-n) Displacement vectors for the three positions corresponding to (e-g and h-j).

Figure

Click here to download high resolution image

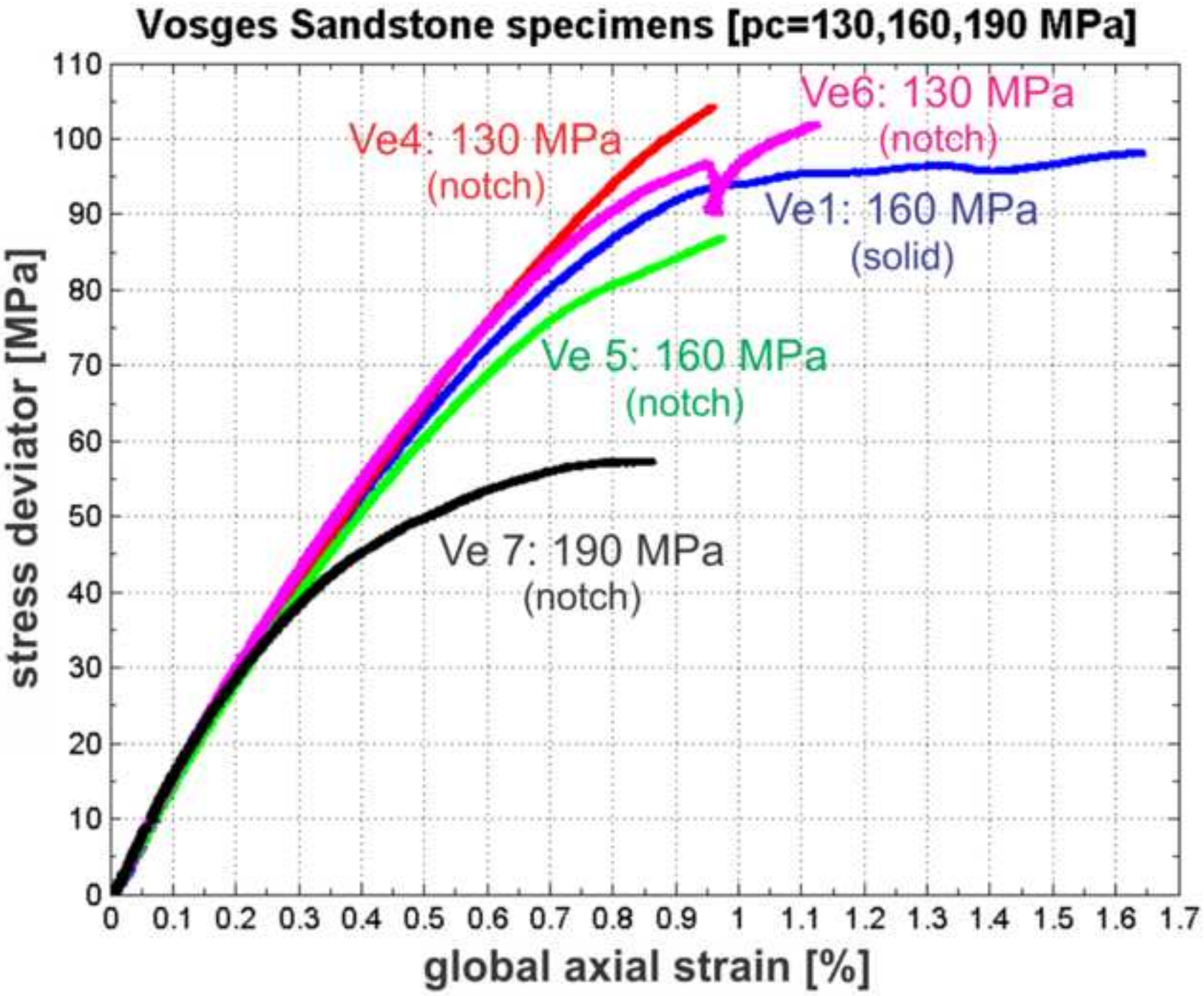

Figure

Click here to download high resolution image

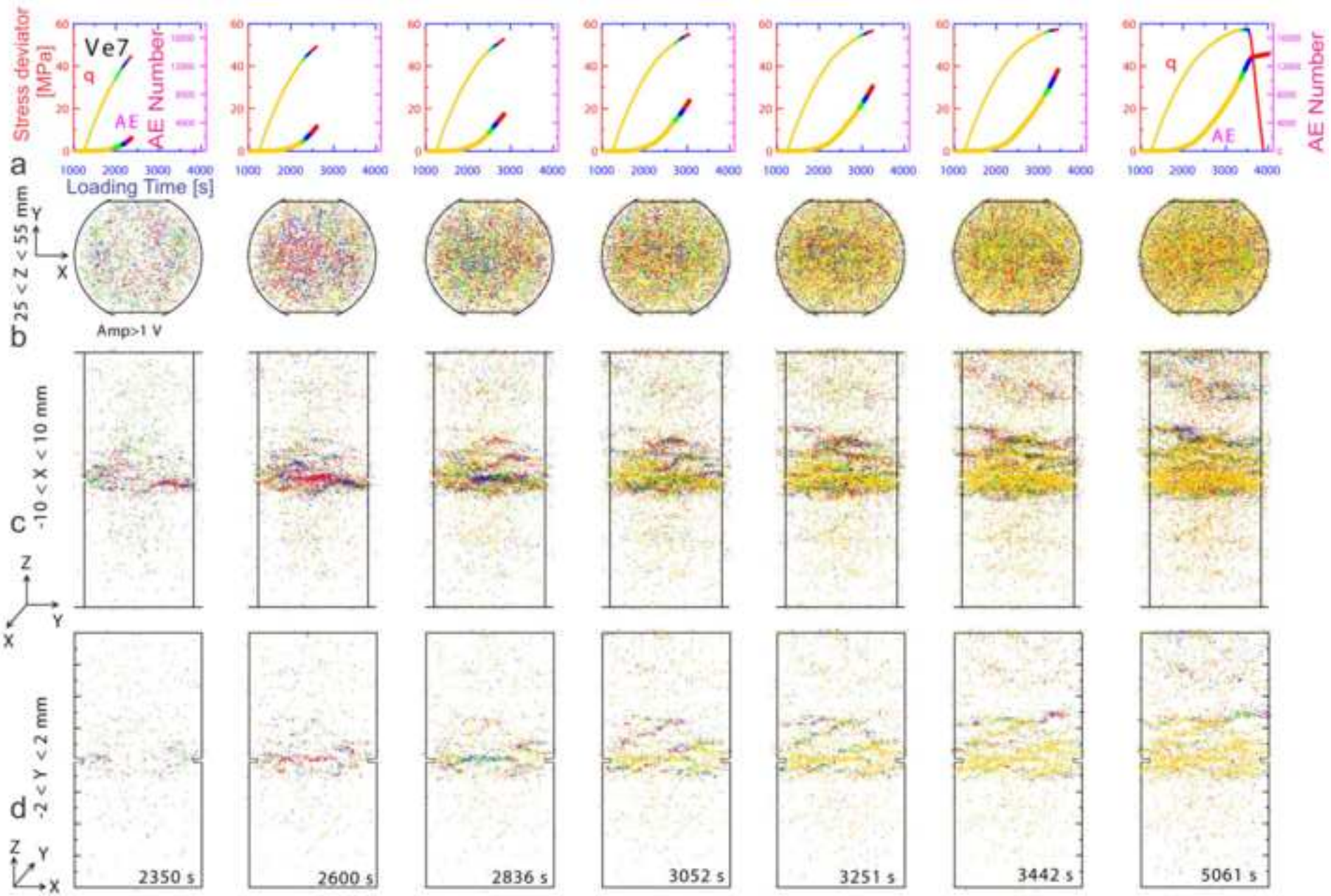

Figure

Click here to download high resolution image

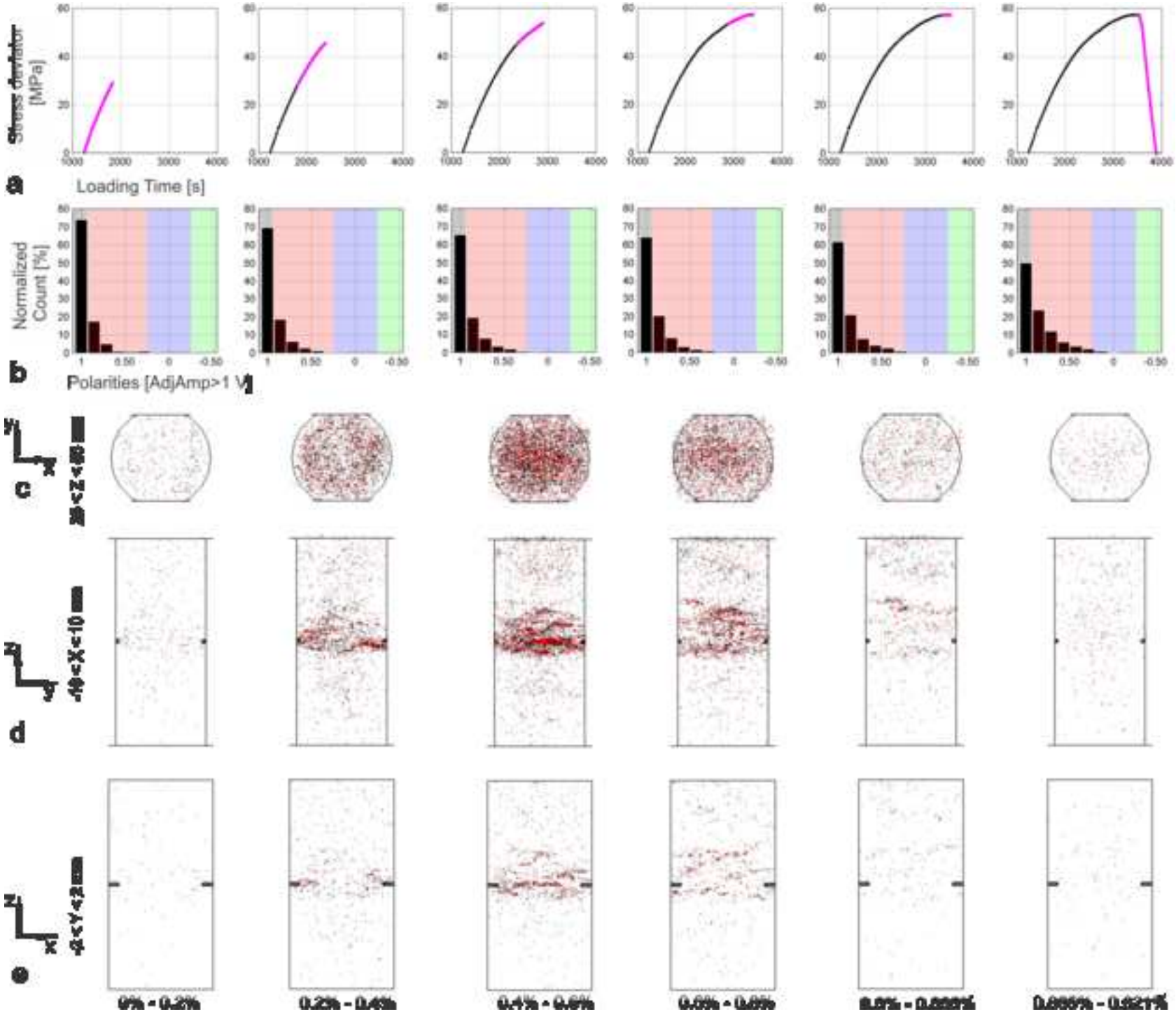

Figure

Click here to download high resolution image

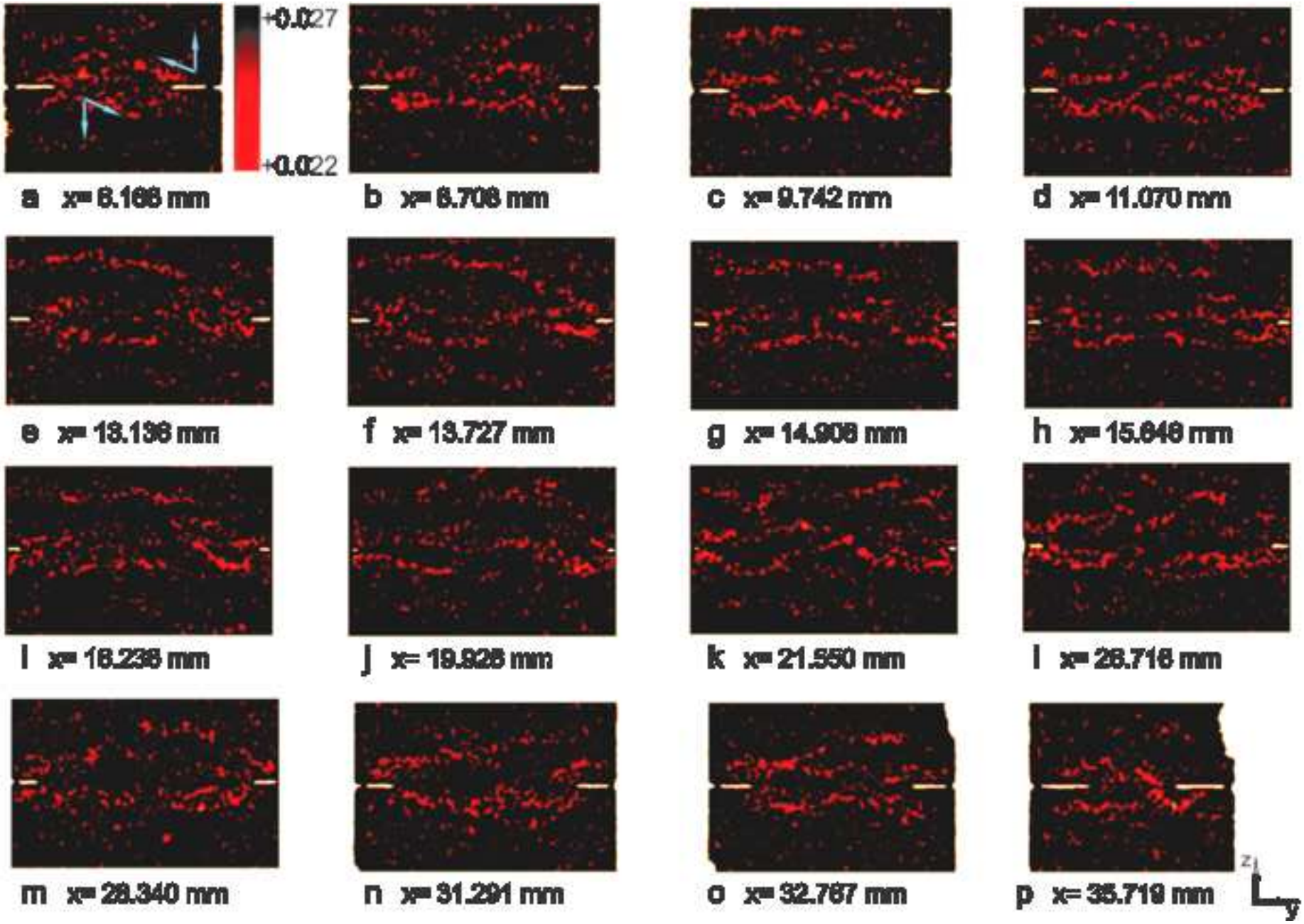

Figure

Click here to download high resolution image

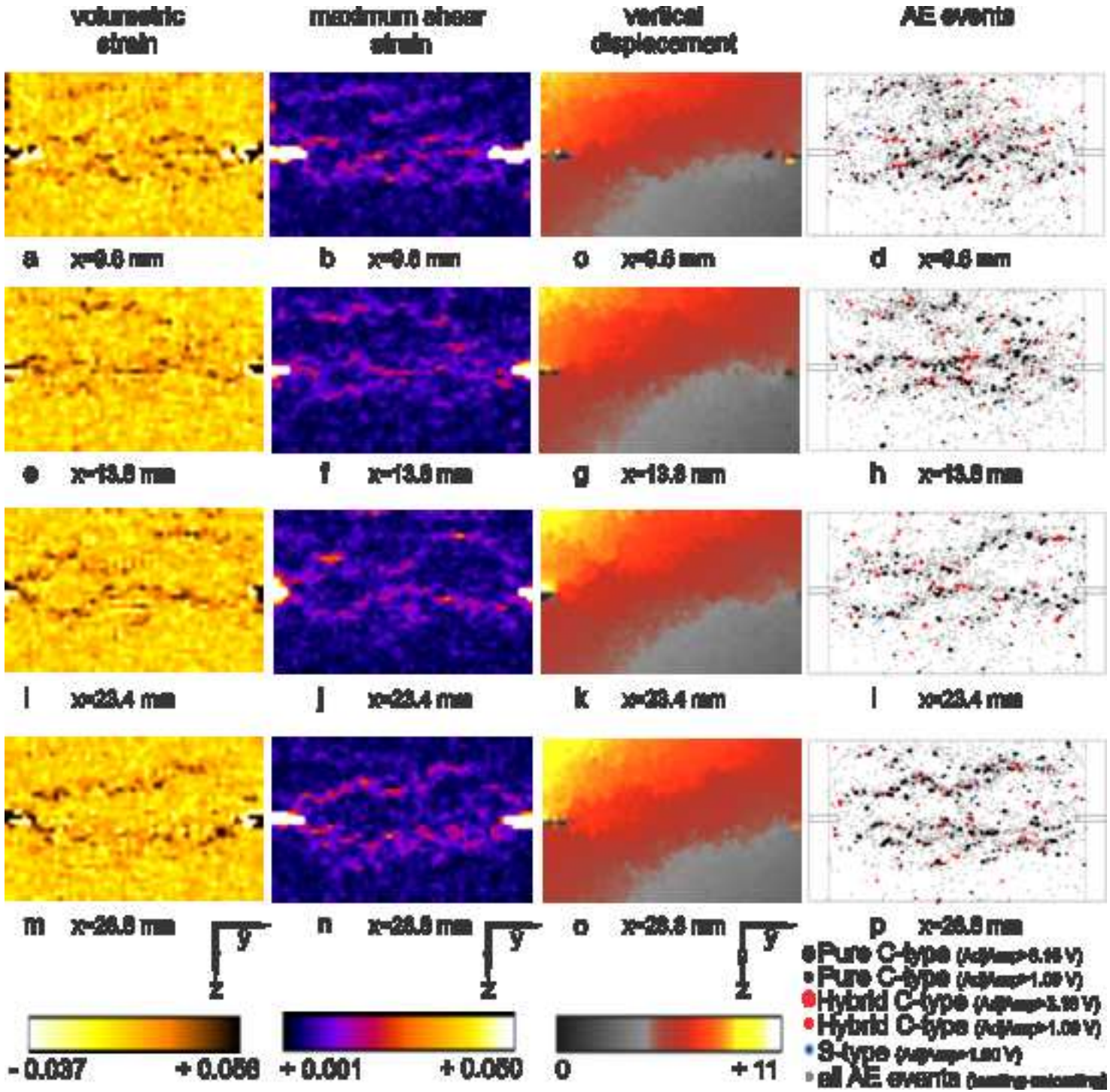

Figure

Click here to download high resolution image

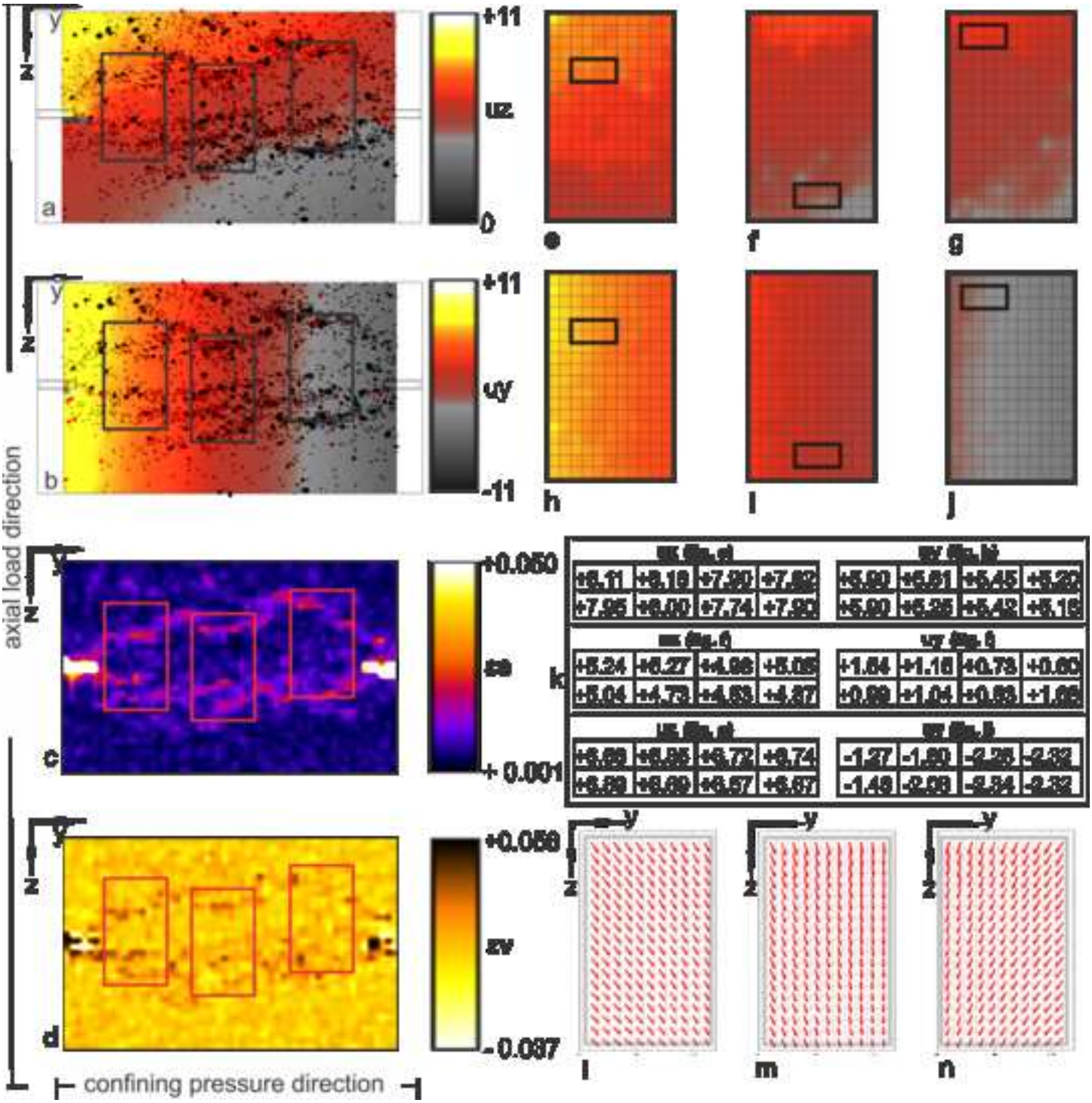

Figure

Click here to download high resolution image

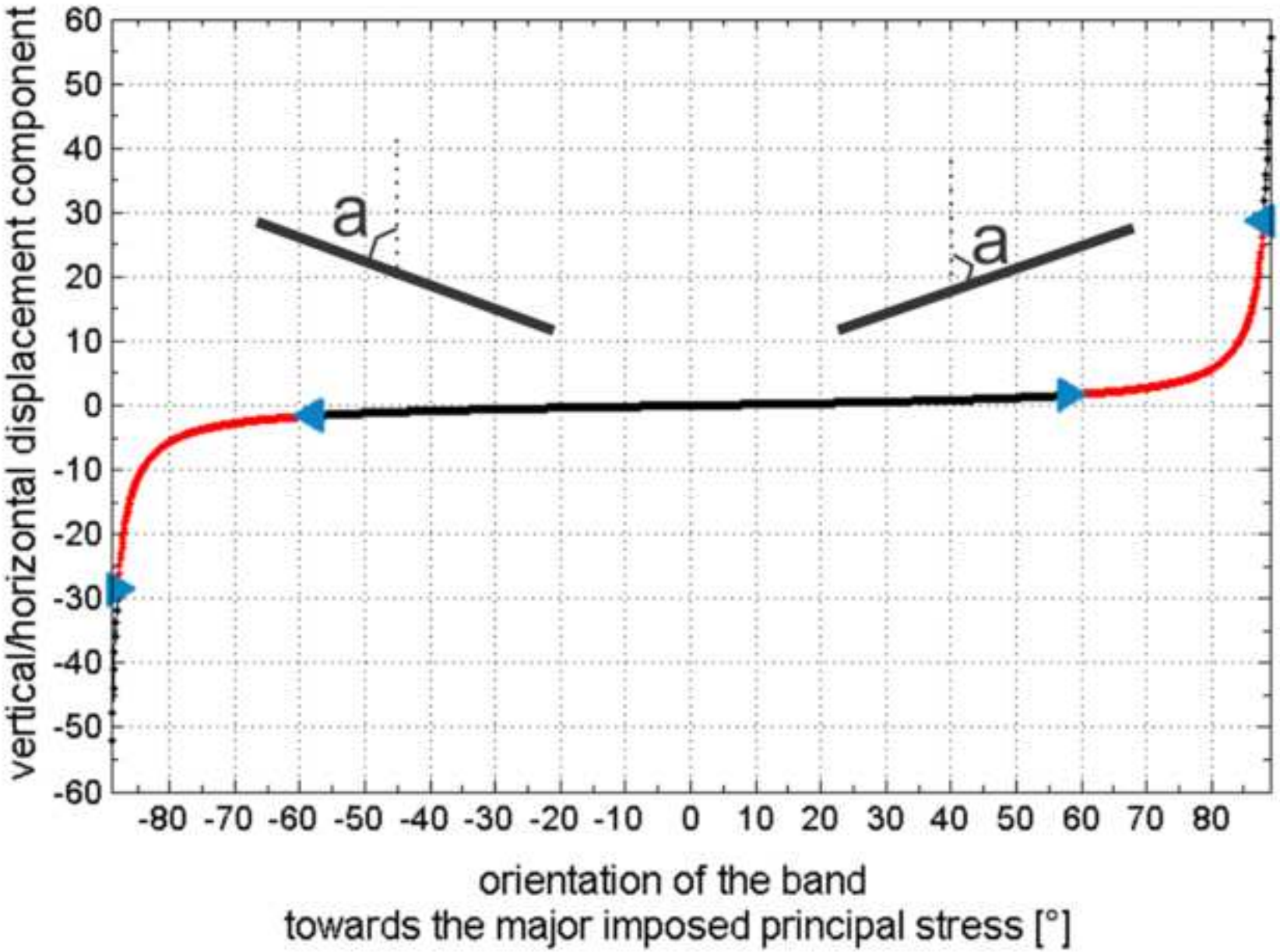

Figure

Click here to download high resolution image

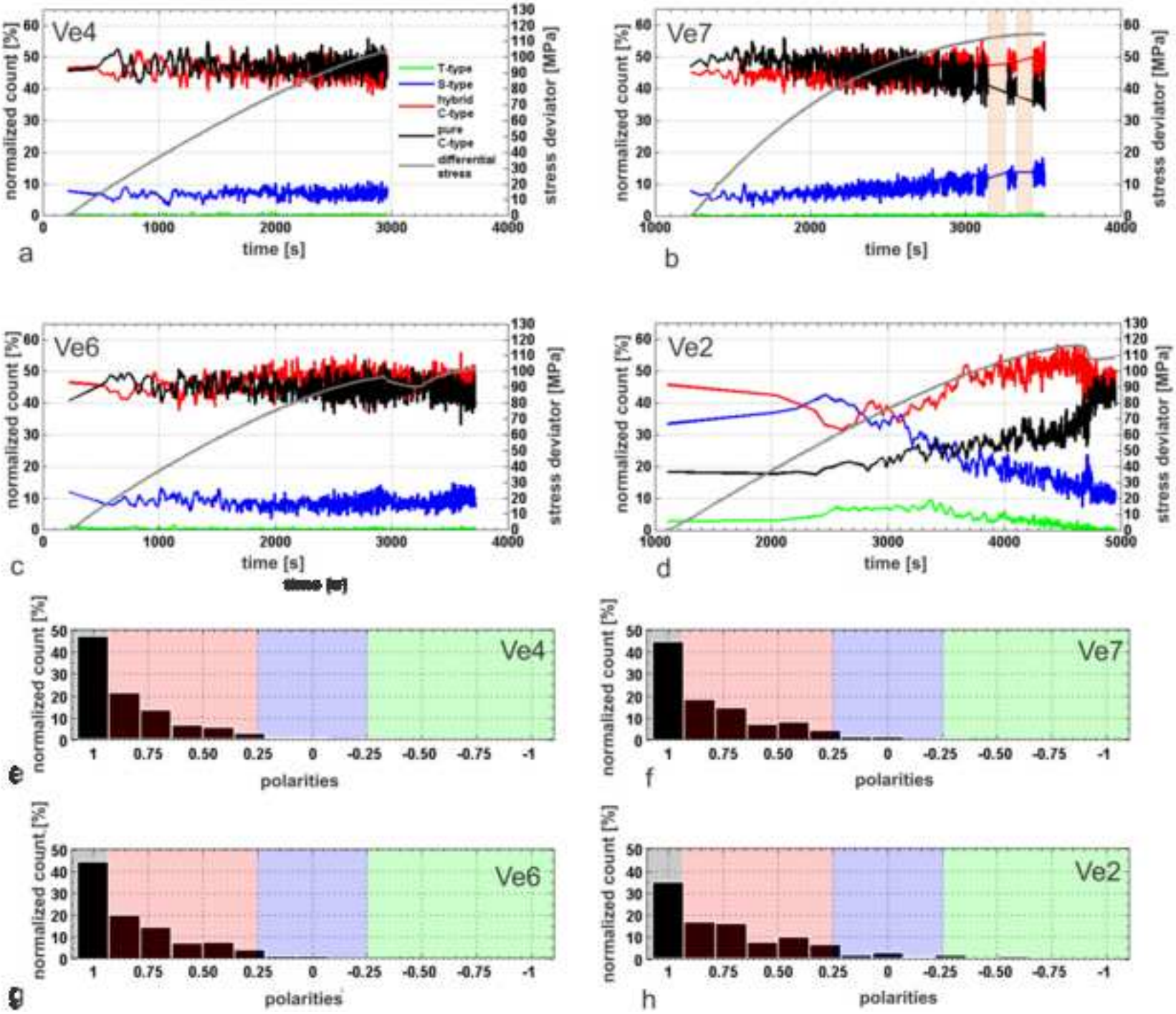

Figure

Click here to download high resolution image